Bulk ablation of soft tissue with intense ultrasound: Modeling and experiments

T. Douglas Mast,[a] Inder Raj S. Makin,[b] Waseem Faidi, and Megan M. Runk
Ethicon Endo-Surgery, 4545 Creek Rd., Cincinnati, Ohio 45242

Peter G. Barthe and Michael H. Slayton
Guided Therapy Systems, 33 S. Sycamore St., Mesa, Arizona 85202

(Received 22 December 2004; revised 1 July 2005; accepted 11 July 2005)

Methods for the bulk ablation of soft tissue using intense ultrasound, with potential applications in the thermal treatment of focal tumors, are presented. An approximate analytic model for bulk ablation predicts the progress of ablation based on tissue properties, spatially averaged ultrasonic heat deposition, and perfusion. The approximate model allows the prediction of threshold acoustic powers required for ablation *in vivo* as well as the comparison of cases with different starting temperatures and perfusion characteristics, such as typical *in vivo* and *ex vivo* experiments. In a full three-dimensional numerical model, heat deposition from array transducers is computed using the Fresnel approximation and heat transfer in tissue is computed by finite differences, accounting for heating changes caused by boiling and thermal dose-dependent absorption. Similar ablation trends due to perfusion effects are predicted by both the simple analytic model and the full numerical model. Comparisons with experimental results show the efficacy of both models in predicting tissue ablation effects. Phenomena illustrated by the simulations and experiments include power thresholds for *in vivo* ablation, differences between *in vivo* and *ex vivo* lesioning for comparable source conditions, the effect of tissue boiling and absorption changes on ablation depth, and the performance of a continuous rotational scanning method suitable for interstitial bulk ablation of soft tissue. © *2005 Acoustical Society of America.* [DOI: 10.1121/1.2011157]

PACS number(s): 43.80.Sh, 43.80.Gx, 43.35.Wa [FD] Pages: 2715–2724

I. INTRODUCTION

Thermal ablation using intense ultrasound is a therapy with potential utility for treatment of pathological soft tissues.[1] For many applications, such as the treatment of primary and metastatic liver tumors, a goal of thermal ablation treatments is to reliably cause thermal necrosis in a relatively large tissue volume (e.g., greater than 5 cm diameter, including a safety margin).[2] In current practice, the thermal destruction of large tissue volumes is most commonly performed using radiofrequency (RF) ablation (electromagnetic radiation in the 400–700 kHz range).[3,4]

Intense ultrasound treatment, first proposed in the 1950s,[5,6] has the potential advantages of selectivity, integrated image guidance, and a noninvasive or minimally invasive approach. To date, most effort in this area has concentrated on extracorporeal[7,8] or intracavitary[9,10] high-intensity focused ultrasound (HIFU). A number of analytic[11–14] and numerical[15–20] studies have provided insight into the dynamics of lesion formation in HIFU treatments, including the effects of blood flow cooling,[15,16] acoustic nonlinearity,[16,18–20] cavitation,[17] and thermoacoustic lensing effects.[19,20]

An alternative approach to HIFU, which can allow the faster ablation of large tissue volumes at the expense of minimal invasiveness, is thermal coagulation by intense ultrasound (IUS) using interstitial probes based on ultrasound transducers in cylindrically omnidirectional,[21] planar,[22] and weakly focused[23] configurations. Clinical applications of interstitial intense ultrasound probes have included intraductal treatment of cholangiocarcinoma and papillary carcinoma.[24]

The modeling of interstitial ablation has also been performed using numerical solutions of the bioheat-transfer equation[25] with various methods for simulation of the ultrasound-induced heat deposition.[26–28] Effects considered in these simulations have included the loss of tissue perfusion due to thermal coagulation.[26,28] The effects of coagulation on ultrasound absorption, as measured experimentally,[29,30] have been modeled using both step[26] and piecewise-linear[28] dependence on the ultrasound-induced thermal dose.

Recent developments in transducer technology[31,32] have allowed the construction of miniaturized linear arrays capable of both IUS treatment and B-scan imaging. Although miniaturized array transducers are not capable of the sharp focusing achievable with large HIFU transducers, these arrays can effectively ablate tissue in bulk,[32] similar to RF ablation devices but with greater selectivity. Treatment planning and monitoring also benefit from the imaging capability of such arrays.

[a]Current address: Department of Biomedical Engineering, University of Cincinnati, Cincinnati, Ohio 45267-0586. Electronic mail: doug.mast@uc.edu
[b]Current address: Guided Therapy Systems, 33 S. Sycamore St., Mesa, Arizona 85202.

In this paper, approaches to the ablation of large tissue volumes using minimally invasive ultrasound probes are presented. A simple analytic model for bulk tissue ablation is presented and compared with experimental results for *ex vivo* and *in vivo* bulk ablation of mammalian liver tissue. Compared to full numerical models of bulk ablation such as those in Refs. 26–28 and the second model presented here, this simple analytic model provides a more convenient means to predict power requirements for thermal ablation under given source and tissue conditions. The analytic model can also be employed to predict differences between *in vivo* and *ex vivo* ablation results for comparable source conditions.

Methods for the detailed simulation of ultrasonic heat deposition and tissue ablation are presented. Intense ultrasound beams, simulated using a Fresnel approximation, induce tissue heating that is modeled using a three-dimensional finite-difference simulation. The heat deposition pattern is adaptively modified based on changes in tissue temperature and thermal dose. Unlike previous numerical models of bulk ablation using ultrasound,[26–28] these methods account for the effect of tissue vaporization on the ultrasound heat deposition. This effect is shown to be important for the realistic prediction of bulk ultrasound ablation. Comparisons of simulated and experimental results show that these simulation methods can effectively predict the depth, rate, and volume of ultrasonic ablation, and thus are a useful tool for the design of therapeutic approaches.

The effect of tissue boiling and absorption changes on ablation depth is illustrated by a matching experiment and simulation. An example bulk ablation method designed to minimize these effects, based on continuous rotational (interstitial) transducer scanning is presented. This method is shown in simulation and experiments to allow the ablation of significant volumes of soft tissue.

II. THEORY

This paper addresses the bulk ablation of soft tissue using intense ultrasound. As a starting point, basic requirements for bulk ablation can be considered. Most previous analytic modeling for ultrasonic tissue ablation has concentrated on highly focused situations,[11–14] for which perfusion effects are limited and beam geometries are very different from unfocused or weakly focused cases. Below, a simple analysis is given that illustrates power requirements for bulk tissue ablation and differences between *in vivo* and *in vitro* ablation experiments.

The bio-heat transfer equation,[25] which is a heat diffusion equation with an added term for perfusion losses, can be written as

$$\rho C\frac{\partial T'}{\partial t} = Q + \kappa\nabla^2 T' - wC_b T', \tag{1}$$

where T' is the tissue temperature rise over its equilibrium temperature T_∞, Q is the power deposited per unit volume, ρ is the tissue mass density, C is the tissue-volume specific heat, w is the blood mass flow rate per unit tissue volume, C_b is the blood-volume specific heat, and κ is the tissue thermal conductivity. For bulk tissue ablation employing broad ultrasound beams, the induced temperature rise will be slowly varying in space, and the thermal conduction term can be neglected to a first approximation. An approximate bioheat equation suitable for simple analytic study can then be written as

$$\frac{\partial T'}{\partial t} \approx \frac{Q}{\rho C} - \frac{1}{\tau}T', \tag{2}$$

where the characteristic perfusion time τ is defined as

$$\tau = \rho C/(wC_b). \tag{3}$$

To obtain an approximate solution for thermal lesioning using Eq. (2), one can assume that all tissue properties are spatially uniform, constant in time, and unchanged by the thermal treatment. For an infinite medium, Eq. (2) then has the solution

$$T' = \frac{Qt}{\rho C}\frac{1-e^{-t/\tau}}{t/\tau}. \tag{4}$$

The quotient $(1-e^{-t/\tau})/(t/\tau)$ reduces to unity for $t/\tau \to 0$ (short treatment times or negligible perfusion) and to τ/t for $t/\tau \to \infty$ (long treatment times).

Equation (4) can be used to illustrate requirements for bulk tissue ablation using intense ultrasound therapy. For heating caused in soft tissue by an arbitrary ultrasound field, the power deposited per unit volume is approximated by $\alpha\langle|p(z)|^2\rangle/(\rho c)$, where α is the acoustic absorption in Nepers per unit length, $\langle\cdot\rangle$ denotes temporal averaging, and c is the speed of sound. This model for heat deposition assumes that acoustic absorption in tissue is due to thermal relaxation.[33]

In order to obtain a simple estimate of requirements for bulk ablation, spatially averaged ultrasound heat deposition may be considered as the heat source in Eq. (4). Since the model results should not depend strongly on the geometry of the ultrasound beam, a general, slowly varying ultrasound field can be approximated for the present purposes as an exponentially attenuated plane wave. The acoustic pressure magnitude $|p(z)|$ is equal to $p_0 e^{-\alpha z}$, where z is the depth of penetration into the tissue and p_0 is the pressure amplitude at the tissue surface. A nominal value for the average heat deposition can be obtained by spatially averaging the acoustic heat deposition over the region where $|p|^2 > \epsilon|p_0|^2$, where ϵ is a parameter less than unity. In the present work, the parameter ϵ was taken to be 0.05, so that for an exponentially attenuated plane wave this region corresponds to the depth range $0 < z < 3/(2\alpha)$. The temporally and spatially averaged heat deposition is then given by

$$Q \sim \frac{\alpha}{\rho c}\left[\langle|p_0|^2\rangle\frac{2\alpha}{3}\int_0^{3/2\alpha} e^{-2\alpha z}\,dz\right] = 0.634\alpha\langle I_0\rangle, \tag{5}$$

where the bracketed term is the spatial average of $|p|^2$ over the depth considered and I_0 is the plane-wave intensity $p_0^2/(2\rho c)$.

For simplicity, it may be assumed that tissue ablation occurs at a threshold temperature T_{thresh}. The minimum acoustic amplitude needed for bulk ablation can then be estimated as the amplitude needed to raise the tissue temperature to its ablation threshold within its characteristic perfu-

sion time $t=\tau$. Inserting the heat deposition from Eq. (5) into Eq. (4) with $t\rightarrow\tau$ yields the threshold amplitude

$$\langle I_0\rangle_{\text{thresh}} \sim \frac{(T_{\text{thresh}}-T_\infty)\rho C}{0.4\alpha\tau}. \tag{6}$$

Representative parameters for human liver tissue *in vivo* are $T_{\text{thresh}}=60\ ^\circ\text{C}$, $T_\infty=37\ ^\circ\text{C}$, $\alpha=5.76\ \text{Np/m/MHz}^{1.2}$, $\rho=1060\ \text{kg/m}^3$, $C=3600\ \text{J/kg/}^\circ\text{C}$, $C_b=3720\ \text{J/kg/}^\circ\text{C}$, $w=18.7\ \text{kg/m}^3\text{/s}$, and $\kappa=0.524\ \text{W/m/}^\circ\text{C}$.[34,35] The resulting characteristic perfusion time is $\tau=55$ s.

For a frequency of 3 MHz and a transducer duty cycle of 75%, the pulsed source intensity required for ablation is thus about $25\ \text{W/cm}^2$. Analogous thresholds for nonplanar ultrasound fields can be obtained from the spatial and temporal average of the acoustic intensity within the region of significant heat deposition, taken here to be the region where the acoustic intensity magnitude is greater than 5% of the spatial peak value.

The simple analysis employed here can also be used to illustrate differences between *in vivo* and *in vitro* ablation experiments. The primary differences affecting ablation performance are differences in perfusion and starting temperature. For example, the formation of a particular ablative lesion *in vitro* may require an exposure of duration t_{vitro}. If the same ultrasonic transducer configuration and power are used for *in vitro* and *in vivo* exposures, the time required to achieve the same ablation *in vivo* can be estimated from Eq. (4) with $\tau\rightarrow\infty$ (no perfusion) for the *in vitro* case. The result is

$$t_{\text{vivo}} = -\tau\log\left(1-\frac{T_{\text{thresh}}-T_{\text{vivo}}}{T_{\text{thresh}}-T_{\text{vitro}}}\frac{t_{\text{vitro}}}{\tau}\right), \tag{7}$$

where T_{vivo} and T_{vitro} are the starting tissue temperatures for the *in vivo* and *in vitro* cases. The relation defined by Eq. (7) is plotted as the solid line in Fig. 1. For example, taking $T_{\text{thresh}}=60\ ^\circ\text{C}$, $T_{\text{vivo}}=37\ ^\circ\text{C}$, $T_{\text{vitro}}=25\ ^\circ\text{C}$, and the tissue parameters defined previously, Eq. (7) predicts that source conditions producing ablation in about 50 s *in vitro* will produce the same ablation *in vivo*, while a power level that requires more than about 83 s to ablate *in vitro* will produce no ablation *in vivo*.

Similarly, one may estimate the *in situ* source intensity required for ablation *in vivo* within the same exposure time t required *in vitro* as

$$I_{\text{vivo}} = I_{\text{vitro}}\frac{T_{\text{thresh}}-T_{\text{vivo}}}{T_{\text{thresh}}-T_{\text{vitro}}}\frac{t/\tau}{1-e^{-t/\tau}}. \tag{8}$$

The ratio of the source intensity required *in vivo* to that *in vitro* is plotted as the solid line in Fig. 1(b). Because of the higher assumed starting temperature, ablative lesions achievable in very short times (e.g., due to high source intensity) will require less power delivery *in vivo*, while lesions achievable by 3 min exposures *in vitro* will be achievable in the same time *in vivo* only if the delivered power is more than doubled. However, if *in vitro* experiments are performed with a starting temperature $T_{\text{vitro}}=T_{\text{vivo}}$, the achievement of a given ablation condition in the same time will always require greater power *in vivo*.

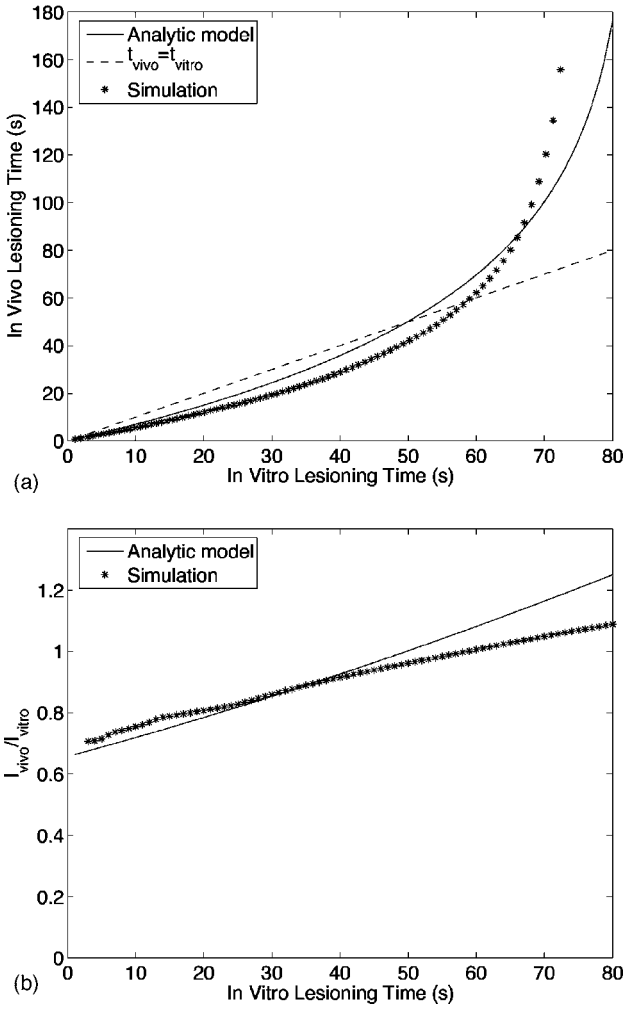

FIG. 1. A comparison of theoretical requirements for *in vitro* and *in vivo* ablation, taking into account blood perfusion and differences in the starting temperature. (a) Time required for *in vivo* and *in vitro* ablation given constant source conditions, estimated from an analytic model and from numerical simulations, shown with the equal-time line (dashed). (b) The ratio between required *in vivo* and *in vitro* source intensities for equal exposure times *in vivo* and *in vitro*, estimated using the analytic model and numerical simulations, and plotted versus exposure time.

These methods can also be used to model bulk ablation using other beam configurations, such as omnidirectional or weakly focused beams, in addition to the nominally planar sources used for most of the results reported here. Whatever the beam configuration, the condition for validity of this analysis is that local heating effects dominate heat conduction effects to a first approximation. Although the above analysis uses a plane wave field as a primary example, Eq. (11) can be used to estimate the appropriate average heat deposition for other transducer configurations, as was done in the analysis reported below in Sec. IV.

III. NUMERICAL METHODS

Heat deposition caused by planar ultrasound transducer arrays was modeled here using the Fresnel approximation for the field of rectangular sources.[36] For simplicity, the medium was assumed to be spatially homogeneous except for a spatially varying absorption coefficient. The total acoustic field was approximated as

$$p(\mathbf{r}) = p_0 \sum_n e^{i\phi n(\mathbf{r_F})} p_n(\mathbf{r}) \int_0^z e^{-\alpha(x,y,\zeta)}\, d\zeta, \tag{9}$$

where $\mathbf{r}$ represents the field point (x,y,z), p_0 is the pressure amplitude at the transducer face, $\alpha(\mathbf{r})$ is the medium attenuation coefficient in Nepers per unit length, $\phi_n(\mathbf{r}_F)$ is the phase shift associated with electronic focusing for the focal point $\mathbf{r}_F$, and $\phi_n(\mathbf{r}_f) = -k|\mathbf{r}_F - \mathbf{r}_n|$, where k is the acoustic wave number. Focusing phase shifts were additionally discretized to multiples of $\pi/8$, in accordance with the phasing capabilities of the electronics employed in the experiments. The field of an individual element centered at position (x_n, y_n) is given under the Fresnel approximation by

$$p_n(\mathbf{r}) = -\frac{ik}{2\pi z \beta^2} e^{ikz} (\mathbf{F}[\beta(x - x_n + a)] - \mathbf{F}[\beta(x - x_n - a)]) \times (\mathbf{F}[\beta(y - y_n + b)] - \mathbf{F}[\beta(y - y_n - b)]), \tag{10}$$

where a is the element half-width in the x (elevation) direction, b is the element half-width in the y (array) direction, $\beta = \sqrt{k/\pi z}$, and the complex Fresnel integral is denoted by $\mathbf{F}[\xi] = \int_0^\xi e^{i\pi\zeta^2/2}\, d\zeta$. The Fresnel integral was evaluated using a fast rational approximation.[37]

Ablation thresholds were computed for array transducers using Eq. (6), with an additional normalization factor accounting for the nonplanar nature of the acoustic fields. The computed acoustic heat deposition was averaged within the volume where the squared pressure was greater than 5% of its maximum value. For consistency with the threshold expressions derived above for plane waves, an effective plane-wave intensity is defined by analogy with Eq. (5) as

$$\langle I_0 \rangle_{\text{eff}} = \frac{1}{0.634 \rho c V_0} \int |p(\mathbf{r})|^2\, dV_0, \tag{11}$$

where the integration volume V_0 covers all points where $|p(\mathbf{r})|^2 > 0.05 \max[|p|^2]$. The factor 0.634 derives from the mean-square amplitude of an exponentially attenuated unit-amplitude plane wave, as in Eq. (5).

To obtain more detailed comparisons between theory and experiment, the bioheat transfer equation (1) was solved in three dimensions using second-order accurate centered differences in space and first-order accurate forward differences in time. The time step for this method was chosen in each case to satisfy the stability condition

$$\Delta t > \frac{\rho C}{2\kappa \left(\frac{1}{(\Delta x)^2} + \frac{1}{(\Delta y)^2} + \frac{1}{(\Delta z)^2} \right) + w C_b}. \tag{12}$$

The heat deposition term was taken to be $Q(\mathbf{r}) = \alpha(\mathbf{r}) |p(\mathbf{r})|^2 / (\rho c)$.[33] The tissue thermal dose[38] was cumulatively calculated in units of equivalent minutes at 43 °C, as

$$\text{EM}_{43}(\mathbf{r}) = \sum R^{T(\mathbf{r}) - 43\,^\circ\text{C}} \Delta t / 60, \tag{13}$$

where Δt is the time step in seconds, $R = 2$ for $T >= 43$ °C, and $R = 4$ for $T < 43$ °C.

Convection boundary conditions were employed at tissue boundaries. Available empirical relations[39] were used to calculate temperature-gradient-dependent convective heat transfer coefficients for water and air media and for vertical and horizontal orientations of the tissue boundaries. The average heat transfer coefficient $\bar{h}$ was assumed to take the form[39]

$$\bar{h} = H \left(\frac{T - T_\infty}{L} \right)^{1/4}, \tag{14}$$

where L is a characteristic length scale, T is the tissue boundary temperature, T_∞ is the free-stream temperature in the surrounding fluid, and H is a constant that depends on the material properties and surface orientation, with dimensions W $\text{m}^{7/4}$ $^\circ\text{C}^{5/4}$. Values of the constant H employed for water bath, *ex vivo* conditions were 194.5 for vertical surfaces, 178.0 for upward-facing horizontal surfaces with $T \geqslant T_\infty$, and 89.0 for upward-facing horizontal surfaces with $T < T_\infty$. For downward-facing horizontal surfaces, conditions for the two values of H are reversed. For air boundaries, the corresponding values of H are 1.4 for vertical surfaces, 1.32 for upward-facing horizontal surfaces with $T \geqslant T_\infty$, and 0.59 for upward-facing horizontal surfaces with $T < T_\infty$.

For the case of rotational scanning, the flow of cooling water in the coupling balloon was accounted for using a constant-temperature boundary condition $T = 15$ °C at the interface of the coupling balloon and the tissue. This boundary condition corresponds to the assumption that the cooling system is sufficient to remove all heat conducted into the cooling fluid from the ultrasound applicator and the surrounding tissue.

Changes in tissue absorption associated with ablation were incorporated in a manner similar to that of Ref. 28, using an empirical formula consistent with available experimental data on the thermal-dose dependence of ultrasonic absorption in mammalian liver tissue:[29]

$$\alpha = \begin{cases} \alpha_0, & \text{EM}_{43} < \text{EM}_0, \\ \alpha_0 \left(1 + \dfrac{\text{EM}_{43} - \text{EM}_0}{\text{EM}_1 - \text{EM}_0} \right), & \text{EM}_0 \leqslant \text{EM}_{43} \leqslant \text{EM}_1, \\ 2\alpha_0, & \text{EM}_{43} > \text{EM}_1, \end{cases} \tag{15}$$

so that the absorption rises linearly to twice its original value between two thermal dose thresholds, taken here to be $\text{EM}_0 = 200$ equivalent minutes and $\text{EM}_1 = 10^7$ equivalent minutes. The form of Eq. (9) allowed this absorption correction to be performed at each time step of the bioheat simulation, without recalculation of the full acoustic field.

Tissue boiling is known to cause substantial changes in acoustic heat deposition, including the shifting of heat deposition toward the ultrasonic source and limiting depth of ablation.[40,41] To account for these effects, a simple model for acoustic shadowing and the redistribution of thermal energy was employed. In Ref. 18, these effects were modeled for single HIFU lesions by assuming that, after any grid point (usually near the acoustic focus) reached a temperature of 100 °C, all of the thermal energy originally deposited in the half-space $z > z_0$ was redistributed in a 0.5 cm spherical region centered around the initial location of tissue boiling. The model employed here extends this idea to more general

heat distributions. Here, when the temperature at any grid point (x_i, y_i, z_i) exceeded 100 °C, the thermal energy deposited along the line $(x=x_i, y=y_i, z>z_i)$ was deposited in a cubic region with 2 mm sides, centered at the point (x_i, y_i, z_i). This operation was performed at each time step for all points exceeding 100 °C at that time, and the redistributed thermal energy sources associated with each location of tissue boiling were superposed. In one implementation of tissue boiling modeling, the temperature at each boiling point can be held constant at 100 °C until the energy deposited after boiling exceeds the latent heat of vaporization of water. However, since use of the latent heat model did not significantly change the numerical results, and since the boiling of a pure liquid may not fully model the boiling of tissue, the latent heat model was not used in the simulations reported here.

To model scanned exposures, the bioheat equation was first solved for the initial ultrasonic exposure. The acoustic heat deposition field was then spatially rotated or translated to the next position, and the bioheat simulation was further iterated using the previous temperature distribution as an initial condition. Corrections for absorption changes and tissue boiling were performed in the same manner at each time step.

IV. RESULTS

Ablation experiments were performed using the methods described in Ref. 32. These included *in vivo* exposures performed on porcine liver as well as *ex vivo* exposures performed on porcine and bovine liver. A variety of miniaturized ultrasound probes were employed, including the image-treat arrays described in Ref. 32 as well as other arrays and single-element, therapy-only transducers. All transducers were driven using tone-burst excitation with acoustic power between 8–60 W and duty cycles between 60%–100%. Single-element transducers were driven by a signal generator and radiofrequency amplifier, while array transducers were driven by a custom electronics system capable of both imaging and therapy.[32] *Ex vivo* experiments were performed in room-temperature water bath conditions, while *in vivo* experiments were performed in open surgical procedures. For the *in vivo* experiments, ultrasound arrays were inserted into actively water-cooled applicators that were applied directly to the liver tissue, either superficially or interstitially. After each experiment, thermal lesions were sliced, photographed, and quantitatively evaluated for ablation depth, volume, and rate.[32]

Intensity thresholds computed using Eqs. (6) and (11) were retrospectively compared with 54 *in vivo* ablation experiments performed in porcine liver with various single-element and array probes operating at frequencies between 2.8 and 7.6 MHz. These probes included various miniaturized arrays and single-element probes designed for interstitial or laparoscopic deployment, with packaging similar to the array applicator described in Ref. 32. Active dimensions for these transducers ranged between 1.5–5 mm in elevation and 16–48 mm in azimuth, with 1–64 independent elements. Also employed was a 3.95 MHz, spherically focused transducer with rectangular active dimensions of 22×40 mm^2.

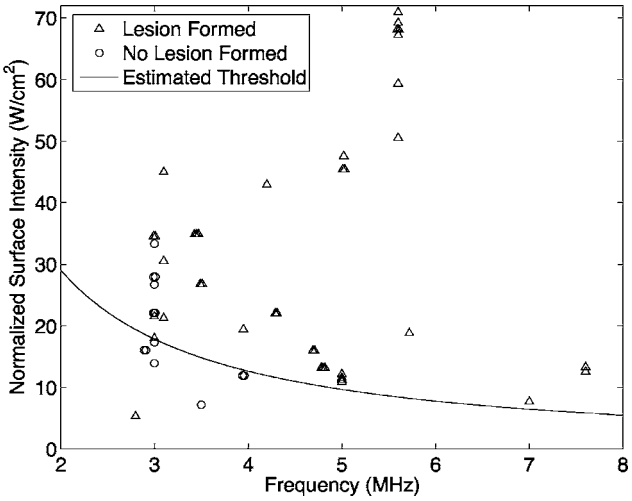

FIG. 2. Theoretical threshold source conditions compared with ablation results from 54 *in vivo* experiments on porcine liver. The smooth curve shows the theoretical time average, equivalent-plane-wave source intensity threshold as a function of frequency. Frequency and normalized source intensity for each experiment are shown using plus symbols where observable lesioning occurred, and open circle symbols where no lesioning occurred.

The theoretical threshold time-average intensity, from Eq. (6) is plotted in Fig. 2 as a function of frequency. Because of increased tissue absorption, intensity requirements for ablation are considerably smaller at higher frequencies. On the same graph, scatter plots show the frequency and normalized (equivalent plane wave) intensity for each of the experiments. Normalized intensity values were obtained using Eq. (11) based on theoretical beam profiles for each source configuration, scaled by surface intensities determined from radiation-force acoustic power measurements.

Those experiments resulting in observable thermal lesioning are plotted in Fig. 2 with plus symbols, while those resulting in no lesioning are plotted with open circles. Observable lesioning was defined here as gross lightening of tissue color due to thermal coagulative denaturation, seen after tissue slicing. For experiments with source conditions below the theoretical lesioning threshold, 7 of 8 produced no lesion. For experiments with source conditions above the theoretical threshold, 39 of 46 produced observable lesions. Thus, in these experiments, the theoretical lesioning threshold corrected the presence or absence of ablation in a majority of cases. However, the range of ablation experimental results available for this retrospective study is not sufficient to rigorously test the ablation threshold model. In general, positive predictions of lesioning may be more challenging than negative predictions, because several experimental unknowns, including tissue motion and probe performance irregularities, can reduce the probability of successful treatment.

To illustrate the differences between *in vitro* and *in vivo* exposures with greater detail, as well as to assess the validity of assumptions made in the analytic ablation modeling described above, numerical simulations were carried out for representative *in vitro* and *in vivo* exposures. The simulated configuration employed a single-element source of frequency 3.0 MHz, active surface dimensions 1.5×25.4 mm^2, and liver tissue with the physical parameters described above,

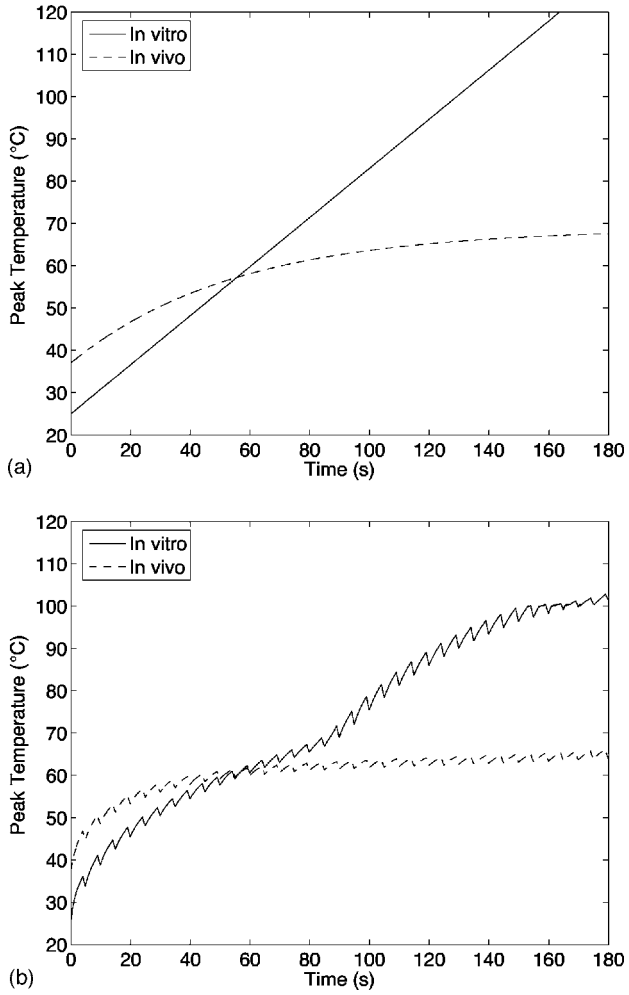

FIG. 3. Peak computed temperature versus time for comparable *ex vivo* (solid lines) and *in vivo* (dashed lines) ablation cases. (a) Approximate analytic model. (b) Finite-difference simulation.

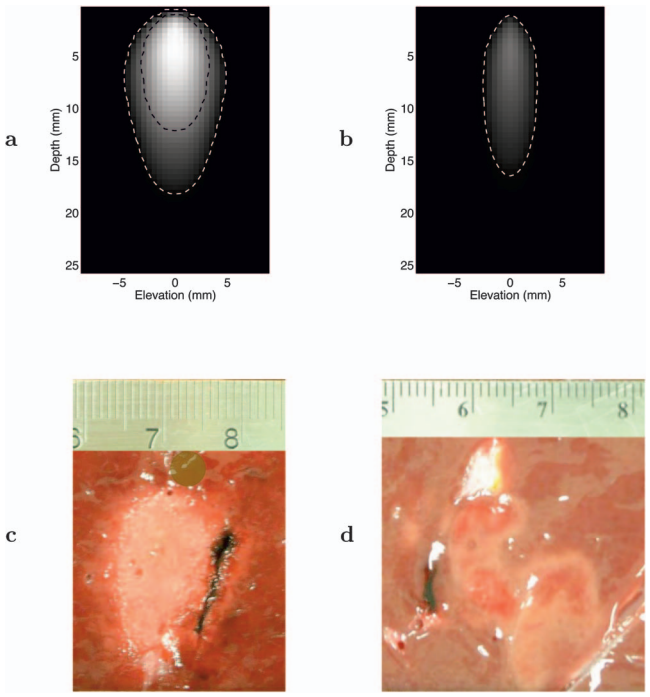

FIG. 4. Ablation *ex vivo* and *in vivo* under comparable exposure conditions. (a) Simulated thermal dose after a 3 min interstitial *ex vivo* exposure, shown on a logarithmic gray scale with superimposed contours at $EM_{43}=200$ and 10^7 equivalent minutes. (b) Simulated temperature after a 3 min *in vivo* exposure. (c) Lesion from a *ex vivo* interstitial exposures at two adjacent angles. The circular overlay indicates the approximate probe position. (d) Lesion from *in vivo* interstitial exposures at seven adjacent locations. The precise probe location is unknown in this case.

and 3 min exposures with an 80% duty cycle (4 s on, 1 s off). The only differences between the *in vitro* and *in vivo* simulations were the starting temperature (25 °C and 37 °C, respectively) and perfusion (zero and 18.7 $kg/m^3/s$, respectively). To ensure that differences between the results depended only on starting temperature and perfusion, identical boundary conditions (convection with coefficients for water at 25 °C, as described previously) were employed in the two cases. For comparison with the analytic model, simulations were performed for surface power densities between 23 and 250 W/cm^2. The time for the onset of ablation, based on a threshold peak temperature of 60°, was determined for each simulation, allowing the comparison of source conditions and ablation times required for *in vitro* and *in vivo* exposures. The results are plotted as individual points in Figs. 1(a) and 1(b). The general agreement with the analytic model confirms the ability of the simpler model to predict ablation trends. The two models differ mainly for long ablation times, greater than about one minute, for which heat conduction plays a more significant role.

More detailed simulation results are shown for this source configuration with a surface power density of 38 W/cm^2, which corresponds most closely to the available experimental data. Simulated time-dependent spatial peak temperatures for the *in vitro* and *in vivo* cases, shown in Fig. 3, show comparable trends for the full numerical approach and the simple analytic model, confirming the validity of the simple analytic model. Both simulations predict that the *in vitro* exposure will cause significant thermal lesioning for the given source conditions, while the comparable *in vivo* exposure will cause little or no lesioning.

Although experimental results exactly analogous to these simulated results are not available, the simulated conditions were similar to those from previous *in vivo* and *in vitro* experiments performed with the same transducer configuration and comparable acoustic power. The *in vitro* experiment used here for comparison employed 2 min exposures at two adjacent angular locations separated by 15° with a power density of about 38 W/cm^2, while the *in vivo* experiment employed seven 3 min exposures at locations separated by 20° with a power density of about 53 W/cm^2. Lesions from the two experiments, shown in Fig. 4 together with the simulated thermal dose for the finite difference simulations, follow the predicted trends. The *ex vivo* lesion is severe, consistent with a temperature rise to ~100 °C and the plotted thermal dose contour at $EM_{43}=10^7$ equivalent minutes, while the *in vivo* lesion shows only regions of coagulation, consistent with a temperature rise to ~60 °C and the plotted thermal dose contour at 200 equivalent minutes. Although these ablation results qualitatively follow the predicted trends, the precise lesion shapes should not be directly

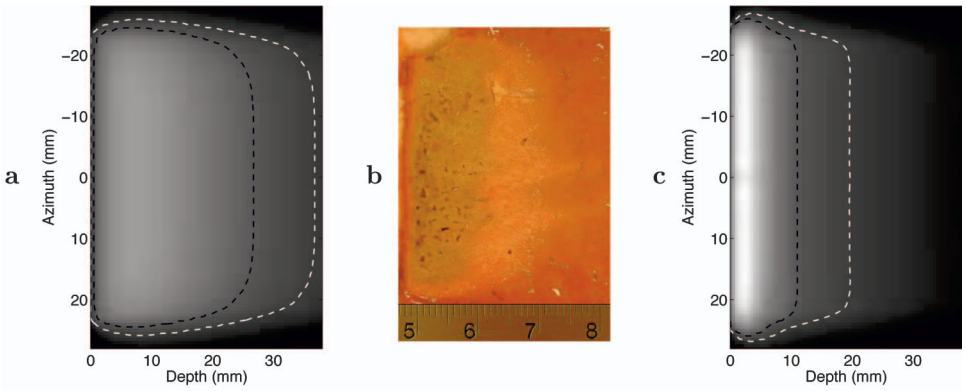

FIG. 5. The effect of boiling and thermal-dose-dependent attenuation. (a) Simulation without boiling and dose-dependent attenuation modeling. The simulated thermal dose is shown on a logarithmic gray scale with superimposed contours at $EM_{43}=200$ and 10^7 equivalent minutes. (b) *Ex vivo* lesion. (c) Simulated thermal dose with boiling and dose-dependent attenuation modeling.

compared with the above simulations because of the different scanning configurations and exposure times employed.

To demonstrate the effect of the present boiling and adaptive attenuation models, simulations were carried out under conditions matching those for an available *ex vivo* experiment, with and without the consideration of boiling and thermal dose-dependent attenuation. The source employed was a 32-element array with dimensions 2.3×49 mm and a frequency of 3.1 MHz, placed 6 mm from the tissue surface. All elements were fired in phase with a surface power density of 39 W/cm^2 for 3 min with an 80% duty cycle (8 s on, 2 s off).

The experimental and simulated results for these ablation conditions, shown in Fig. 5, indicate that the present boiling and adaptive attenuation models effectively characterize the screening effects associated with tissue ablation. The experimental results showed an ablation depth of 10–15 mm for severe ablation (brown and cracked tissue) and 20–25 mm for any ablation (discolored tissue), while the measured ablation rate was 1.92 ml/min. The simulation results with unmodified heat deposition significantly overpredict the depth of ablation (37 mm based on an $EM_{43}=200$ threshold for ablation or 27 mm based on an $EM_{43}=10^7$ threshold for severe ablation) as well as the ablation rate (4.0 ml/min). Results from the simulations including the boiling and adaptive attenuation models show much better agreement with experiment for both the depth of ablation (20 mm based on an $EM_{43}=200$ threshold for ablation or 11 mm based on an $EM_{43}=10^7$ threshold for severe ablation) as well as the ablation rate (2.1 ml/min).

Bulk ablation experiments employing interstitially scanned configurations were also performed. The example illustrated here was performed using a continuous angular scanning configuration that was found to reduce premature proximal tissue ablation, so that the depth-limiting effects illustrated in Fig. 5 were minimized. A 3 mm image-treat array, having 32 elements with an active aperture of 2.3×49 mm and a frequency of 3.1 MHz, was inserted interstitially into an excised lobe of bovine liver. All array elements were simultaneously fired in phase with an acoustic power of 74.3 W and an 80% duty cycle (0.8 s on, 0.2 s off) while the array was rotated by a stepping motor at a rate of 22 s per revolution, the maximum rate available for the motor employed. The active exposure time for these source conditions was 19 min. Since continuous unidirectional rotation is not feasible due to cabling, the probe was alternately rotated clockwise for one revolution and counterclockwise for the next, with each revolution beginning at the same turning point.

To simulate this experiment, a sequence of individual exposures was performed with numerical rotation of the ultrasonic heat deposition field before each exposure. To minimize the computation time while maintaining a smooth rotation of the heating pattern, the angular steps were separated by 10°, so that the exposure time at each step was 0.61 s and a total of 52 rotations were performed to model an exposure time of 19 min. The duty cycle, source intensity, and back-and-forth rotation pattern matched those employed in the experiment. Thus, exposures were alternately performed for the sequence of angular positions 0°, 10°,…,350° and the se-

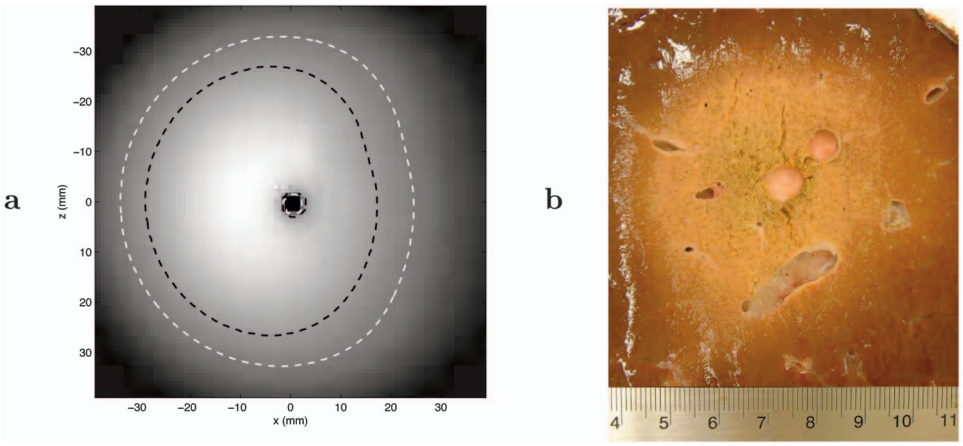

FIG. 6. Thermal lesioning from an *in vitro* continuous-sweep rotational scan. (a) Simulated thermal dose, plotted on a logarithic gray scale, with contours shown for $EM_{43}=200$ and 10^7 equivalent minutes. (b) Cross section of *ex vivo* lesion.

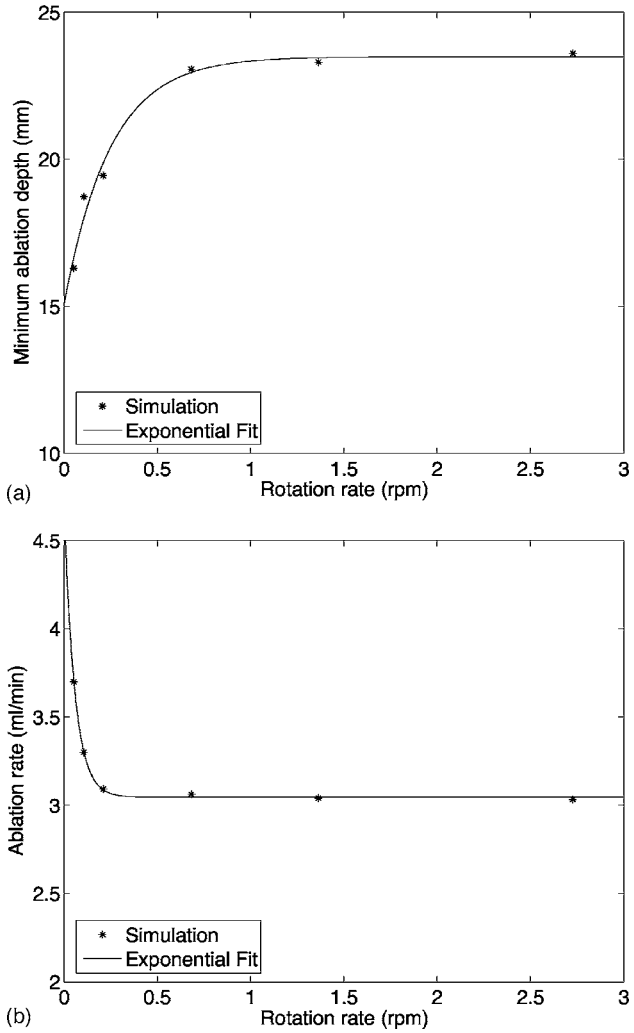

FIG. 7. Simulated effect of rotational scanning rate on interstitial bulk ablation, based on simulations using the configuration of Fig. 6. In both plots, simulated data are shown with exponential fits of the form $y=Ae^{-\Omega\tau}+B$. (a) Minimum ablation depth, measured radially from the transducer axis. (b) Ablation rate.

quence 0°, 350°,…,10°. A cross section of the resulting bulk ablation at the array midpoint is shown in Fig. 6, together with the simulated thermal dose map in the same plane and contours at $EM_{43}=200$ and 10^7 min. The lesion shape and depth are seen to agree fairly well, including the lesser depth ablated near the rotational turning point. An examination of simulated temperature fields suggests that this asymmetry occurs because larger temperature rises initially occur opposite the turning point, resulting in increased tissue absorption [Eq. (15)] and thus greater heat deposition. The simulated volume of ablation, based on an $EM_{43}=200$ min threshold, is 57.8 ml, while the experimentally measured ablation volume was 63.9 ml.

The example illustrated by Fig. 6 employed rapid rotational scanning, with the purpose of maximizing the ablation depth. The effect of the rotation rate on the ablation depth and rate is illustrated further by analogous simulations for a range of rotational speeds. Several simulations were performed for the same configuration as the previous example (Fig. 6), but with reduced rotational speeds corresponding to 1, 2, 4, 13, and 26 rotations within the 19 min treatment duration. The resulting simulated ablation depths and rates are plotted in Fig. 7. The minimum ablation depth, which occurred near the rotational turning point in all cases, was determined by an interpolation of a contour corresponding to a thermal dose $EM_{43}=200$ min, while the ablation rate was determined based on the same thermal dose threshold. As illustrated in Fig. 7, the slowest rotational rates result in larger ablation rates but smaller minimum ablation depths. Both simulated datasets are fit well by curves of the form $y=Ae^{-\Omega\tau}+B$, where Ω, measured in revolutions per minute (rpm), is the rotational scanning rate. Parameters determined by a least-squares fit are $A=-8.41$ mm, $\tau=4.04$ min, $B=23.5$ mm for minimum depth ($r=0.990$), and $A=1.63$ ml/min, $\tau=17.5$ min, $B=3.05$ ml/min for the ablation rate ($r=0.999$). The increased ablation rate for slow scanning rates is due to more rapid local heating, which reduces losses due to heat conduction. The decreased depth for slow scanning rates is due to the boiling and thermal dose-dependent absorption effects illustrated by Fig. 5.

V. DISCUSSION

This work describes methods using intense ultrasound energy to achieve bulk ablation for soft tissue. The simple analytic approach described here allows an estimation of the source and timing conditions required for ablation, while the full numerical approach provides greater detail. The capabilities, limitations, and applications of each of these approaches are discussed below.

The simple analytic approach to bulk ablation modeling presented here effectively assumes a uniform temperature distribution within the region of interest. This model is clearly limited by the neglect of heat conduction, spatial variations in heat deposition, and changes in tissue state due to the thermal treatment. However, comparisons between the analytic model, experimental results, and full numerical simulations suggest that the simple analytic method is useful in defining the source requirements necessary for ablation. The analytic method predicts the differences between *in vivo* and *ex vivo* source conditions needed for ablation, as seen by the comparison with full numerical simulations in Figs. 1 and 3. This method also predicts intensity thresholds for *in vivo* ablation under a variety of probe configurations, as illustrated by Fig. 2.

The prediction success of this analytic approach is possible because, for bulk ultrasonic ablation, perfusion effects are the dominant limiting factor for *in vivo* ablation. While it has previously been established that perfusion can significantly change ablation characteristics for HIFU,[42] perfusion losses play a larger role when less intense (unfocused, planar, or weakly focused) acoustic fields are used to achieve bulk ablation. Although the analytic model breaks down for long-duration exposures in the absence of perfusion, it effectively predicts the trends of temperature time history in perfused tissue.

Full numerical simulations provide a more complete prediction of ablation *ex vivo* and *in vivo*, including the spatial characteristics of ablation. The simulation methods reported here extend previous approaches by incorporating a more

detailed model for heat redistribution due to tissue boiling. Neglected effects include acoustic nonlinearity, temperature-dependent changes in tissue properties other than ultrasonic absorption, and the structural inhomogeneity of tissue. Of these effects, the inhomogeneous structure of tissue is likely to be among the most important. For example, if source conditions are close to the ablation threshold illustrated in Fig. 2, small variations in heat deposition due to refraction and scattering as well as inhomogeneous perfusion losses may cause some areas of tissue to be undertreated while others are overtreated.

In addition, losses of tissue perfusion due to thermal coagulation, which were neglected here, could cause increased heating after initial tissue ablation. These effects could be straightforwardly incorporated into the numerical methods described above by defining a perfusion function specified to be zero at all locations where the thermal dose has exceeded a threshold value, such as the 10^7 equivalent minutes used above as a criterion for severe ablation. Notably, the inclusion of this effect would not change the *in vivo* simulation results presented here (Fig. 4), because the thermal dose did not reach this threshold in that simulation.

The comparisons with experiment reported here indicate that both of the present modeling approaches can be used to predict bulk ablation of soft tissue. An estimation of threshold source amplitudes obtained using the analytic model predicted trends of ablation for *in vivo* ablation experiments under a wide range of source conditions. Ablation results predicted using the full numerical model agreed well with experimentally measured ablation depths, volumes, and rates. To obtain close correspondence between simulated and actual ablation, consideration of temperature- and thermal-dose-dependent changes in heat deposition are important.

Both of the modeling approaches presented here have potential use in guiding further development of devices and methods for the ultrasonic ablation of soft tissue. The analytic approach can be employed to estimate the source conditions required for reliable ablation *in vivo*. This approach also allows the extrapolation of *ex vivo* experimental results, which can be obtained under controlled conditions, to predict ablation effects in living, perfused tissue. The second approach presented here, which includes detailed modeling of acoustic heat deposition and transfer, is suitable for more detailed design of bulk ablation devices, methods, and experiments.

In the present work, use of these models has facilitated the design of source conditions for the improved bulk ablation of liver tissue. Design goals based on ablation as currently performed using RF devices include rapid ablation ($\sim$1.5–2.0 ml/min) and a large depth of ablation ($\sim$30 mm). Scanning schemes such as the continuous rotational scan shown in Fig. 6 and the sweeping linear scan illustrated in Ref. 32 were designed to minimize shadowing effects associated with the ablation of tissue near the acoustic source. As illustrated by Fig. 7, the simulation of a range of scanning configurations can allow the minimization of these shadowing effects, resulting in more uniform ablation of clinically relevant tissue volumes.

VI. CONCLUSIONS

Two approaches to modeling bulk ablation using intense ultrasound have been presented. These approaches include a simple analytic method for a definition of treatment requirements and a more complete simulation method for modeling of the details of ablation. A comparison between the two models confirms that the analytic method predicts trends of source requirements for bulk ablation, with the greatest accuracy for fairly short treatment times (e.g., the achievement of initial ablation within one minute). Comparisons with experiments indicate that the simple analytic model can predict ablation thresholds and approximate heating characteristics of tissue, while the full numerical methods can predict the shape, volume, depth, and rate of ablation effectively. A combination of these techniques is promising for the design of future approaches for bulk ablation of soft tissue.

[1] J. E. Kennedy, G. R. ter Haar, and D. Cranston, "High intensity focused ultrasound: Surgery of the future?" Br. J. Radiol. **76**, 590–599 (2003).
[2] S. N. Goldberg, G. S. Gazelle, and P. R. Mueller, "Thermal ablation therapy for focal malignancy: A unified approach to underlying principles, techniques, and diagnostic imaging guidance," AJR, Am. J. Roentgenol. **174**, 323–331 (2000).
[3] S. A. Curley, "Radiofrequency ablation of malignant liver tumors," Ann. Surg. Oncol. **10**, 338–347 (2003).
[4] R. J. Zagoria, "Percutaneous image-guided radiofrequency ablation of renal malignancies," Radiol. Clin. North Am. **41**, 1067–1075 (2003).
[5] W. J. Fry, "Biological and medical acoustics," J. Acoust. Soc. Am. **30**, 387–393 (1958).
[6] P. P. Lele, "Production of deep focal lesions by focused ultrasound—Currrent status," Ultrasonics **5**, 105–112 (1967).
[7] G. R. ter Haar, D. Sinnett, and I. Rivens, "High-intensity-focused ultrasound: a surgical technique for the treatment of discrete liver tumors," Phys. Med. Biol. **34**, 1743–1750 (1989).
[8] F. Wu, W.-Z. Chen, J. Bai, J.-Z. Zou, Z.-L. Wang, H. Zhu, and Z.-B. Wang, "Pathological changes in human malignant carcinoma treated with high-intensity focused ultrasound," Ultrasound Med. Biol. **27**, 1099–1106 (2001).
[9] A. Gelet, J. Y. Chapelon, R. Bouvier, O. Rouviere, Y. Lasne, D. Lyonnet, and J. M. Dubemard, "Transrectal high-intensity focused ultrasound: minimally invasive therapy of localized prostate cancer," J. Endourol **14**, 519–528 (2000).
[10] T. Uchida, N. T. Sanghvi, T. A. Gardner, M. O. Koch, D. Ishii, S. Minei, T. Satoh, T. Hyodo, A. Irie, and S. Baba, "Transrectal high-intensity focused ultrasound for treatment of patients with stage T1b-2n0m0 localized prostate cancer: a preliminary report," Urology **59**, 394–398 (2002).
[11] J. B. Pond, "The role of heat in the production of ultrasonic focal lesions," J. Acoust. Soc. Am. **47**, 1607–1611 (1970).
[12] T. C. Robinson and P. P. Lele, "An analysis of lesion development in the brain and in plastics by high-intensity focused ultrasound at low-megahertz frequencies," J. Acoust. Soc. Am. **47**, 1607–1611 (1970).
[13] F. L. Lizzi and M. Ostromogilski, "Analytical modelling of ultrasonically induced tissue heating," Ultrasound Med. Biol. **10**, 289–298 (1984).
[14] C. R. Hill, I. Rivens, M. G. Vaughan, and G. R. ter Haar, "Lesion development in focused ultrasound surgery: a general model," Ultrasound Med. Biol. **20**, 259–269 (1994).
[15] M. C. Kolios, M. D. Sherar, and J. W. Hunt, "Blood flow cooling and ultrasonic lesion formation," Med. Phys. **23**, 1287–1298 (1996).
[16] F. P. Curra, P. D. Mourad, V. A. Khoklova, R. O. Cleveland, and L. A. Crum, "Numerical simulations of heating patterns and tissue temperature response due to high-intensity focused ultrasound," IEEE Trans. Ultrason. Ferroelectr. Freq. Control **47**, 1077–1089 (1999).
[17] F. Chavrier, J. Y. Chapelon, A. Gelet, and D. Cathignol, "Modeling of high-intensity focused ultrasound-induced lesions in the presence of cavitation bubbles," J. Acoust. Soc. Am. **108**, 432–440 (2000).
[18] P. M. Meaney, M. D. Cahill, and G. R. ter Haar, "The intensity dependence of lesion position shift during focused ultrasound surgery," Ultrasound Med. Biol. **26**, 441–450 (2000).
[19] I. M. Hallaj and R. O. Cleveland, "Simulations of the thermo-acoustic lens

effect during focused ultrasound surgery," J. Acoust. Soc. Am. **109**, 2245–2253 (2001).
[20]C. W. Connor and K. Hynynen, "Bio-acoustic thermal lensing and nonlinear propagation in focused ultrasound surgery using large focal spots: a parametric study," Phys. Med. Biol. **47**, 1911–1928 (2002).
[21]C. J. Diederich, W. H. Nau, and P. R. Stauffer, "Ultrasound applicators for interstitial thermal coagulation," IEEE Trans. Ultrason. Ferroelectr. Freq. Control **46**, 1218–1228 (1999).
[22]R. Chopra, C. Luginbuhl, A. J. Weymouth, F. S. Foster, and M. J. Bronskill, "Interstitial ultrasound heating applicator for MR-guided thermal therapy," Phys. Med. Biol. **46**, 3133–3145 (2001).
[23]C. Lafon, D. M. de Lima, Y. Theillière, F. Prat, J.-Y. Chapelon, and D. Cathignol, "Optimizing the shape of ultrasound transducers for interstitial thermal ablation," Med. Phys. **29**, 290–297 (2002).
[24]F. Prat, C. Lafon, D. M. de Lima, Y. Theilliere, J. Fritsch, G. Pelletier, C. Buffet, and D. Cathignol, "Endoscopic treatment of cholangiocarcinoma and carcinoma of the duodenal papilla by intraductal high-intensity US: Results of a pilot study," Gastrointest Endosc **56**, 909–915 (2002).
[25]H. H. Pennes, "Analysis of tissue and arterial blood temperatures in the resting human forearm," J. Appl. Physiol. **1**, 93–122 (1948).
[26]C. Lafon, F. Prat, J. Y. Chapelon, F. Gorry, J. Margonari, Y. Theillere, and D. Cathignol, "Cylindrical thermal coagulation necrosis using an interstitial applicator with a plane ultrasonic transducer: *in vitro* and *in vivo* experiments versus computer simulations," Int. J. Hyperthermia **16**, 508–522 (2000).
[27]R. Chopra, M. J. Bronskill, and F. S. Foster, "Feasibility of linear arrays for interstitial ultrasound thermal therapy," Med. Phys. **27**, 1281–1286 (2000).
[28]P. D. Tyreus and C. J. Diederich, "Theoretical model of internally cooled interstitial ultrasound applicators for thermal therapy," Phys. Med. Biol. **47**, 1073–1089 (2002).
[29]C. A. Damianou, N. T. Sanghvi, F. J. Fry, and R. Maass-Moreno, "Dependence of ultrasonic attenuation and absorption in dog soft tissues on temperature and thermal dose," J. Acoust. Soc. Am. **102**, 628–634 (1997).
[30]A. E. Worthington and M. D. Sherar, "Changes in ultrasound properties of porcine kidney tissue during heating," Ultrasound Med. Biol. **27**, 673–682 (2001).
[31]P. G. Barthe and M. H. Slayton, "Efficient wideband linear arrays for imaging and therapy," *1999 IEEE Ultrasonics Symposium Proceedings*, Vol. **2**, pp. 1249–1252.
[32]I. R. S. Makin, T. D. Mast, W. Faidi, M. M. Runk, P. G. Barthe, and M. H. Slayton, "Miniaturized ultrasound arrays for interstitial ablation and imaging," Ultrasound Med. Biol. (in press).
[33]W. L. Nyborg, "Heat generation by ultrasound in a relaxing medium," J. Acoust. Soc. Am. **70**, 310–312 (1981).
[34]International Commission on Radiation Units and Measurements, *ICRU Report 61: Tissue Substitutes, Phantoms and Computational Modeling in Medical Ultrasound* (ICRU Publications, Bethesda, MP, 1998).
[35]F. A. Duck, *Physical Properties of Tissue: a Comprehensive Reference Book* (Academic Press, London, 1990).
[36]A. Freedman, "Sound field of a rectangular piston," J. Acoust. Soc. Am. **32**, 197–209 (1960).
[37]M. Abramowitz and I. A. Stegun, *Handbook of Mathematical Functions* (National Bureau of Standards, Washington DC, 1972), Chap. 7.
[38]S. A. Sapareto and W. C. Dewey, "Thermal dose determination in cancer therapy," Int. J. Radiat. Oncol., Biol., Phys. **10**, 787–800 (1984).
[39]J. P. Holman, *Heat Transfer*, 7th ed. (McGraw-Hill, New York, 1990), Chap. 7.
[40]N. A. Watkin, G. R. ter Haar, and I. Rivens, "The intensity dependence of the site of maximal energy deposition in focused ultrasound surgery," Ultrasound Med. Biol. **22**, 483–491 (1996).
[41]W.-S. Chen, C. Lafon, T. J. Matula, S. Vaezy, and L. A. Crum, "Mechanisms of lesion formation in high intensity focused ultrasound therapy," ARLO **4**, 41–46 (2003).
[42]A. Arafiev, F. Prat, J. Y. Chapelon, J. Tavakkoli, and D. Cathignol, "Ultrasound-induced tissue ablation: studies on isolated, perfused porcine liver," Ultrasound Med. Biol. **24**, 1033–1043 (1998).